Molecular Dynamics of the Long Neurotoxin LSIII†

Peter J. Connolly,*,‡,§ Alan S. Stern,‡ Christopher J. Turner,‖ and Jeffrey C. Hoch*,‡,⊥

Rowland Institute at Harvard, 100 Edwin H. Land Boulevard, Cambridge, Massachusetts 02142, and Francis Bitter Magnet Laboratory, Massachusetts Institute of Technology, 150 Albany Street, Cambridge, Massachusetts 02139

Received April 29, 2003; Revised Manuscript Received August 20, 2003

ABSTRACT: Long neurotoxins bind tightly and specifically to the nicotinic acetylcholine receptor (AChR) in postsynaptic membranes and are useful for exploring the biology of synapses. In crystallographic studies of long neurotoxins the principal binding loop appears disordered, but the NMR solution structure of the long neurotoxin LSIII revealed significant local order, even though the loop is disordered with respect to the globular core. A possible mechanism for conferring global disorder while preserving local order is rigid-body motion of the loop about a hinge region. Here we report investigations of LSIII dynamics based on $^{13}C_\alpha$ magnetic relaxation rates and molecular dynamics simulation. The relaxation rates and MD simulation both confirm the hypothesis of rigid-body motion of the loop and place bounds on the extent and time scale of the motion. The bending motion of the loop is slow compared to the rapid fluctuations of individual dihedral angles, reflecting the collective nature and largely entropic free energy profile for hinge bending. The dynamics of the central binding loop in LSIII illustrates two distinct mechanisms by which molecular dynamics directly impacts biological activity. The relative rigidity of key residues involved in recognition at the tip of the central binding loop lowers the otherwise substantial entropic cost of binding. Large excursions of the loop hinge angle may endow the protein with structural plasticity, allowing it to adapt to conformational changes induced in the receptor.

LSIII belongs to the family of long neurotoxins that bind with high affinity and specificity to the nicotinic acetylcholine receptor (AChR)[1] (*1*). Isolated from the venom of the green sea snake *Laticauda semifasciata*, LSIII inhibits binding of acetylcholine (ACh) to AChR in the postsynaptic membranes of nerves and skeletal muscle, preventing the flow of cations across the membrane and transmission of nerve impulses. To gain insights into the molecular basis for the affinity and specificity of long neurotoxins for AChR, we previously determined the three-dimensional structure of LSIII in solution using nuclear magnetic resonance (NMR) spectroscopy (*2*). In contrast to structures of related proteins determined by X-ray crystallography, the structure revealed a locally well-ordered central binding loop that is disordered relative to the rest of the protein. Here we report the results of investigations into the loop dynamics using measurement of ^{13}C nuclear magnetic relaxation rates and molecular dynamics (MD) simulation. The results confirm that there is quasi-rigid-body motion of the binding loop with respect to the core of the protein, consistent with conclusions reached from the solution structure determination. Together, the empirical relaxation results and MD simulation reveal the character of the loop dynamics, including bounds on the rate and extent of structural fluctuations, and illustrate two distinct mechanisms by which molecular dynamics can influence biological activity.

Long and short neurotoxins share a common structural motif (depicted in Figure 1) consisting of a three-stranded antiparallel β-sheet and three loops protruding from a globular core. Neurotoxins are cysteine-rich, with four disulfide bonds stabilizing the globular core; in long neurotoxins, a fifth disulfide linkage is located in the central loop. The central loop contains a number of residues that are highly conserved and essential for high binding affinity to the receptor (*1*). In crystallographic studies of the long neurotoxins α-cobratoxin (*3*) and α-bungarotoxin (*4*) the electron density for the central binding loop is diffuse, indicating static or dynamic disorder. The ensemble of solution structures of α-cobratoxin based on nuclear Overhauser effects (NOEs) and vicinal coupling constants measured by NMR (*5*) exhibited large variations in the conformation of the central loop, with large root-mean-square displacements (RMSDs) of the atoms in the central loop. The central loop (loop II) in the ensemble of solution structures determined for LSIII (*2*) also has large backbone RMSDs but is locally ordered. In contrast to structure determination based on X-ray diffraction, NMR structures are based on geometric constraints derived from local, short-range interactions and are thus capable of revealing local order even when the local frame of reference is disordered

† This work was supported by the Rowland Institute for Science and by grants from the National Institutes of Health (GM-47467 and RR-00995) and the National Science Foundation (MCB 9527181).

* Address correspondence to these authors.

‡ Rowland Institute at Harvard.

§ Present address: UCB Research Inc., 840 Memorial Drive, Cambridge, MA 02139.

‖ Massachusetts Institute of Technology.

⊥ Present address: Department of Microbial, Molecular, and Structural Biology, University of Connecticut Health Center, 263 Farmington Ave., Farmington, CT 06030-3305.

[1] Abbreviations: AChR, acetylcholine receptor; NMR, nuclear magnetic resonance; NOE, nuclear Overhauser effect; MD, molecular dynamics; RMS, root mean square.

10.1021/bi034687m CCC: $25.00
Published on Web 11/15/2003

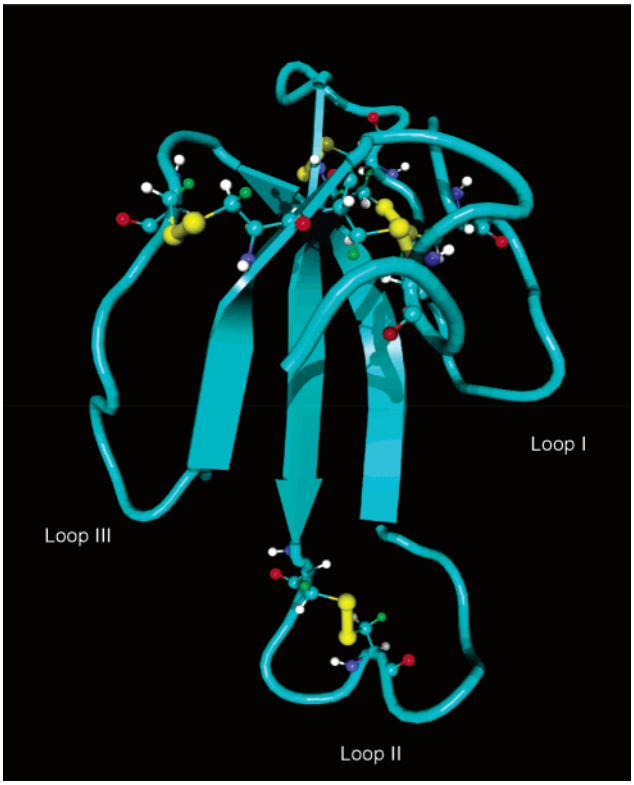

FIGURE 1: Cartoon representation of the structure of LSIII based on NMR (*2*). Side chain atoms for the cysteine residues are shown, with the disulfide bonds shown in yellow.

with respect to other parts of the protein. NOEs as well as scalar coupling constants from loop II of LSIII clearly indicate the presence of local order, suggesting that the disorder seen in crystallographic studies of homologous proteins results from disorder of the loop with respect to the crystallographic reference frame (and the core of the protein).

Large backbone RMSDs in solution structure ensembles result from a lack of structural constraints of which molecular dynamics is only one possible cause (coincidental overlap of spectral resonances is another) and do not unequivocally indicate molecular motion (*6*). Studies of magnetic relaxation induced by dipole−dipole interaction in $^{13}C-^{1}H$ or $^{15}N-^{1}H$ spin pairs can directly detect motion responsible for large fluctuations in backbone conformation, provided that the motion is fast relative to the overall molecular tumbling (*7*).

The contribution of molecular dynamics to binding free energy has been well-established both for enzyme catalysis (*8*) and for molecular recognition by proteins (*9*). Mutagenesis of the Cys residues forming the bridging disulfide bond of loop II in bungarotoxin results in a 14-fold reduction of its affinity for the α7 subunit of neuromuscular AChR (*10*). The side chains for these residues are located opposite the face of loop II known to interact with α7, so the reduction is consistent with an increase of the configurational entropy of the free neurotoxin that is lost upon binding. Consequently, investigation of the molecular dynamics of long neurotoxins will improve our understanding of their biological activity.

The results of magnetic relaxation experiments and molecular dynamics (MD) simulation we present here support the hypothesis, based originally upon the NMR solution structure ensemble, that the dynamics of the principal binding loop of LSIII can be described as rigid-body motion about a hinge region. The finding has clear implications for the thermodynamics of LSIII biding to AChR, as the entropic cost of binding an ordered loop is lower than that for a disordered loop (*9*). Entropy also plays a role in the dynamics of the loop motion, as fluctuations of the hinge angle involve collective fluctuations of several dihedral angles. In light of evidence that AChR undergoes conformational change upon binding agonists (*11*, *12*) and neurotoxins (*13*, *14*), a possible biological role for the loop dynamics is to permit the protein to remain bound as the receptor undergoes conformational change.

MATERIALS AND METHODS

Sample Preparation. LSIII was purchased from Sigma Chemical Co. and used without further purification. The protein was dissolved in D_2O at pH 7.0 and left to stand for several days to allow the labile protons to exchange. After the solution was lyophilized, samples were prepared in 99.9% D_2O, and the pH was adjusted to 4.6 (uncorrected for isotope effects) by the addition of DCl and NaOD; this pH was used in the structural studies (*2*). Investigation of the binding affinity of bungarotoxin found no difference between acidic and neutral pH (*15*).

NMR Spectroscopy. All experiments were performed using a custom-built spectrometer at the Francis Bitter Magnet Laboratory operating at 591.02 MHz ^{1}H frequency. All spectra were acquired at 25 °C, with 1024 and 128 complex points in the acquisition and indirect time dimensions, respectively, using a recycle delay of 3 s. Samples contained ^{13}C at natural abundance, and with a nominal protein concentration of 3 mM, 400 transients per t_1 increment were required to achieve adequate signal-to-noise ratio. For each spectrum, the ^{1}H carrier was positioned at 4.75 ppm relative to an internal DSS reference and the ^{13}C carrier at 50.0 ppm, with carbon chemical shifts calculated from the proton frequencies according to Wishart et al. (*16*). The spectral widths were 16.6 ppm (^{1}H) and 67.5 ppm (^{13}C) in f_2 and f_1, respectively. Natural abundance PEP-PFG ^{13}C HSQC spectra were acquired using a modification of the pulse sequence described by Kay et al. (*17*). Two-dimensional $^{1}H-^{13}C$ HSQC-TOCSY spectra were acquired using a pulse sequence incorporating coherence selection gradients and PEP (*18*) with *z*-filtered DIPSI-2 isotropic mixing times of 20, 40, and 60 ms. R_1, R_2, and $^{13}C\{^{1}H\}$ NOE data were acquired using the pulse sequences described by Skelton et al. (*19*) modified to include coherence selection gradients (*20*). Cross-correlation between dipolar and chemical shift anisotropy relaxation mechanisms was suppressed by the application of ^{1}H π pulses every 2 ms during the relaxation period for the R_1 spectra and by the CPMG scheme for the R_2 spectra (*21*, *22*). Eight spectra were acquired for the R_1 measurements with relaxation delays of 0.02, 0.05, 0.1, 0.2, 0.3, 0.5, 1.0, and 1.5 s, and seven spectra were obtained for the R_2 measurements with delays of 0.002, 0.008, 0.016, 0.024, 0.032, 0.048, and 0.064 s. Proton saturation for the NOE experiments was achieved using a train of 3 kHz, 120 deg pulses every 5 ms. For the unsaturated spectrum, the pulse train was applied with the proton carrier moved 400 kHz off resonance to minimize the effects of differential sample heating.

Spectra were processed using the Rowland NMR Toolkit (*23*, *24*). A 10 Hz exponential line broadening was applied in both dimensions, and the data were zero-filled to 2048 ×

2048 points prior to Fourier transformation. Peak picking, resonance assignment, and peak quantification were performed using XEASY (*25*). The longitudinal relaxation rates were determined by nonlinear least-squares fit of the experimental data to a single-exponential function describing the inversion−recovery

$$I(t) = I_\infty - (I_\infty - I_0)\exp(-R_1 t) \quad (1)$$

and the transverse relaxation rates to a single-exponential decay of the form

$$I(t) = I_0 \exp(-R_2 t) \quad (2)$$

using the program CURVEFIT (*26*). NOEs were obtained as the ratio of the saturated to unsaturated peak intensities. Errors in the experimental resonance intensities were estimated from the RMS noise in blank regions of the two-dimensional spectra, and propagated errors in the relaxation rates were determined by Monte Carlo simulation as described by Mandel et al. (*27*).

The amplitudes and time scales of the internal molecular motions were estimated from the relaxation data using the "model-free" formalism of Lipari and Szabo (*28*), using the program MODELFREE 3.1 (*29*). The theory behind the model-free formalism has been described extensively in the literature (for reviews see refs *7*, *29*, and *30*), and we shall not discuss it here. After a preliminary estimate for the overall rotational correlation time τ_m was obtained from R_1/R_2 ratios as described by Kay et al. (*21*), three different dynamical models were fit to the data for each residue while the value of τ_m was held fixed. The first (model 1) included only the order parameter S^2. Model 2 included an additional parameter τ_e describing the time scale of internal motion, and model 3 included a third parameter, the exchange term R_{ex}. A grid search was used to obtain initial values of the adjustable parameters for the final fit, and model selection was carried out as described by Mandel et al. (*27*). The final parameter values and error estimates were determined by fitting the relaxation data to the selected model for each residue, allowing the overall correlation time to vary.

Hydrodynamics Calculations. Rotational correlation times were calculated from the solution structure closest to the mean using the program HYDRO (*31*), using one bead with a radius of 1 Å for each heavy atom. Solvent viscosities of 0.0089 and 0.0109 g/cm·s were used for H_2O and D_2O, respectively (*32*).

Molecular Dynamics Calculations. Molecular dynamics simulations were performed using AMBER 4.1 (*33*) running on a Silicon Graphics Power Challenge computer with a protocol similar to that of Fox and Kollman (*34*). The force field of Cornell et al. (*35*) was used, and nonbonded electrostatic terms were treated using the particle-mesh Ewald method (*36*) with a charge grid spacing of approximately 1 Å. Nonbonded van der Waals interactions were evaluated normally, with an 8 Å cutoff. The solution structure nearest to the average of the ensemble of structures (*2*) was minimized and solvated in a box of SPC/E water (*37*) with dimensions of 67.7 Å × 57.6 Å × 51.3 Å. The entire system was then subjected to a series of minimizations, constraining the protein backbone atoms to their original positions with force constants of 1000, 100, 50, 15, 2, and 0 kcal/mol. Short simulations were carried out at 100 and 200 K prior to the run used for analysis. The analysis simulation was carried out under conditions of constant temperature (300 K) and pressure (1 atm) and with periodic boundary conditions. The temperature was regulated as described by Berendsen et al. (*38*), using a time constant of 0.2 ps. SHAKE (*39*) was used to constrain bond lengths involving hydrogen atoms, permitting an integration time step of 1.5 fs. Prior to analysis, overall rotation of the protein was removed by least-squares alignment of all 66 C_α backbone atoms. Angular order parameters, used to characterize the breadth of dihedral angle distributions, were computed as described by Hyberts et al. (*40*). Angular correlation functions were computed using the formula

$$C_{ang}(\tau) = \frac{1}{N-\tau}\sum_{t=0}^{N-\tau-1}\cos(\theta_t - \theta_{t+\tau}) \quad (3)$$

where N is the total number of time steps in the trajectory.

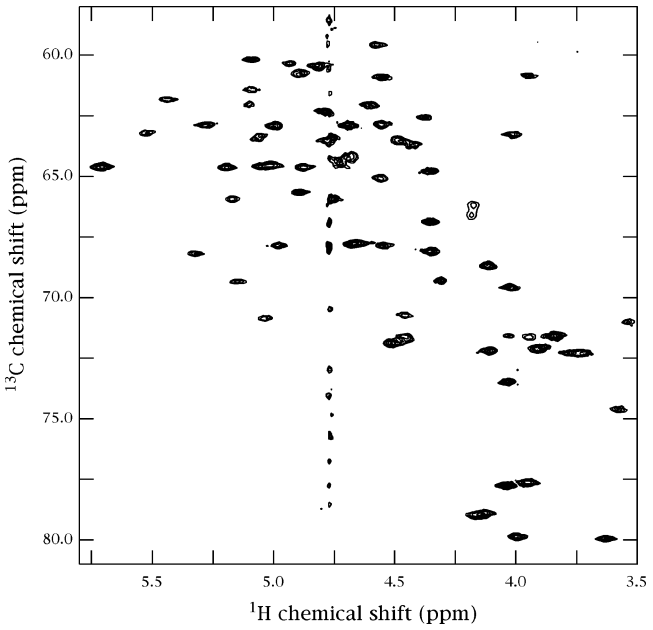

FIGURE 2: $H_\alpha-C_\alpha$ region of the natural abundance ^{13}C HSQC spectrum of LSIII acquired at 25 °C, pH 4.6.

RESULTS AND DISCUSSION

Resonance Assignments. Forty out of 66 C_α resonances were unambiguously assigned on the basis of a natural abundance $^1H-^{13}C$ HSQC spectrum and the previously assigned α-protons (*2*). An additional 11 assignments were made from a series of pseudo-two-dimensional natural abundance $^1H-^{13}C$ HSQC-TOCSY spectra (*41*) using $C_\alpha-$side chain proton correlations to resolve ambiguities due to degenerate H_α chemical shifts. Of the 51 assigned C_α resonances, four were from glycines and six were poorly resolved, resulting in 41 C_α resonances suitable for relaxation analysis. The assignments are given in Table 1 of the Supporting Information.

R_1, R_2, and NOE. Figure 2 shows a part of the $C_\alpha-H_\alpha$ region from one of the two-dimensional heteronuclear correlation spectra used to determine R_1. Spectra for the determination of R_2 were of similar quality. Figure 3 shows the dependence of cross-peak intensity on the relaxation delay

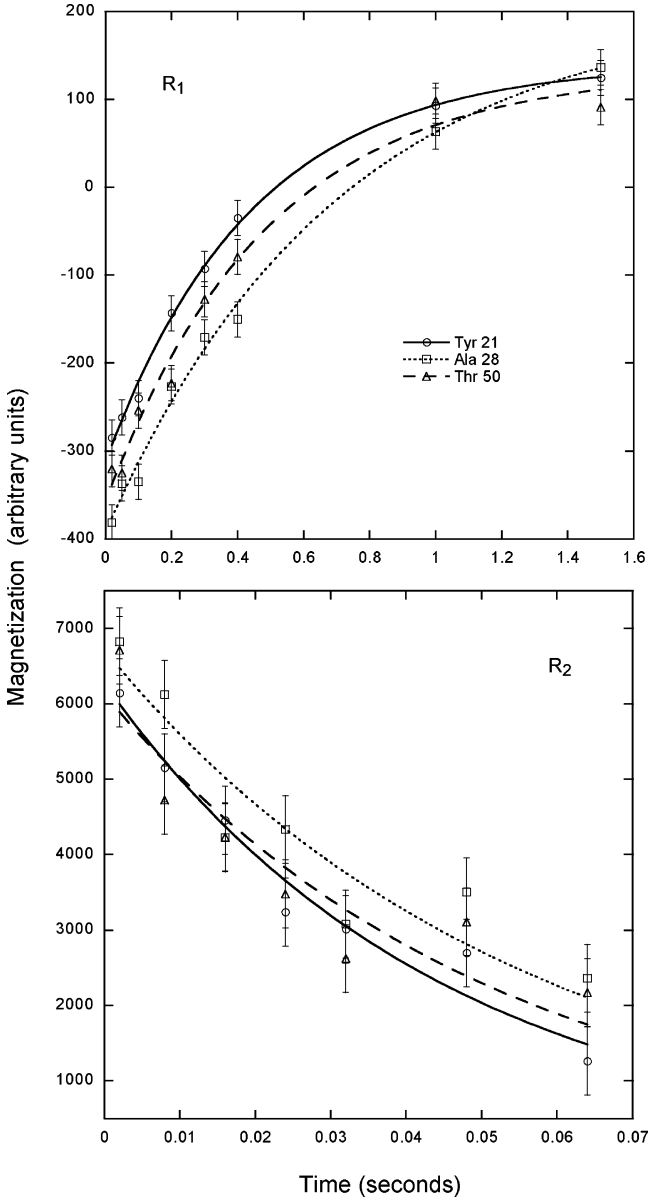

FIGURE 3: Representative data obtained from the measurement of longitudinal (R_1) and transverse (R_2) ^{13}C relaxation rates for Tyr 21 (○), Ala 28 (□), and Thr 50 (△). Errors were estimated from the RMS noise in blank regions of the spectra. Fits to the data (as described in the text) are shown by the lines.

time as well as the least-squares fit of the relaxation rates R_1 and R_2 to the data for representative $C_\alpha-H_\alpha$ resonances. Nearly all of the data fit satisfactorily to the single exponentials of eqs 1 and 2. A few residues gave fits to the data with a χ^2 statistic significantly exceeding the critical value corresponding to the 95% confidence interval. These resonances were near the residual HDO peak, suggesting that the RMS noise is underestimated for this region of the spectrum. The average uncertainty in the relaxation parameters was 14% for R_1 and 9% for R_2. The sum of χ^2 values was substantially lower than the value expected for the 95% confidence interval, indicating that the uncertainties in the relaxation parameters are, on average, overestimated. The uncertainty in the $^{13}C\{^1H\}$ NOE was estimated at 20% from the RMS noise level in the saturated and unsaturated spectra. The R_1, R_2, and $^{13}C\{^1H\}$ NOE values are given in Figure 4 and in Table 1 of the Supporting Information.

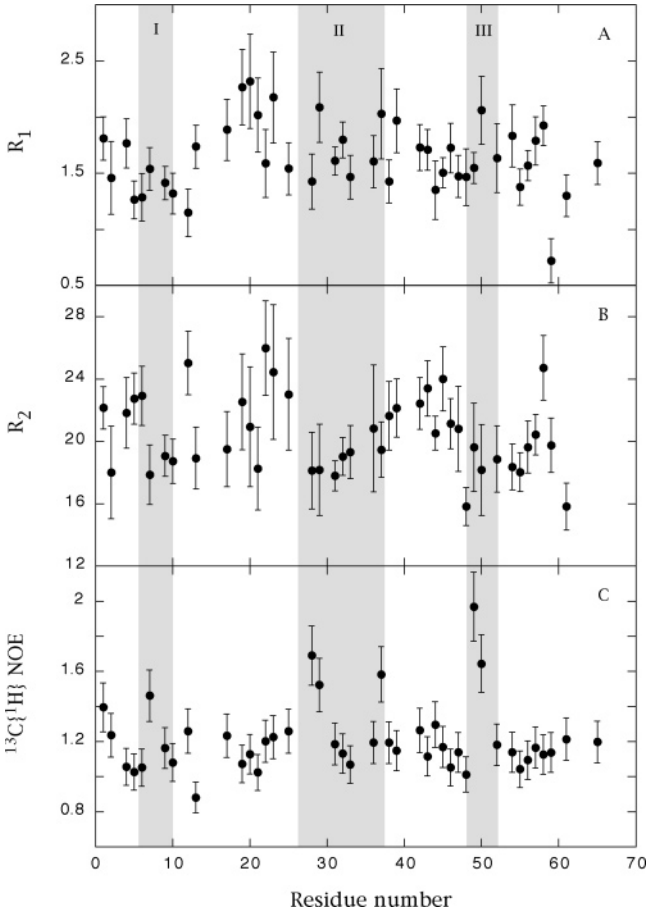

FIGURE 4: $^{13}C_\alpha$ relaxation rates R_1 and R_2 and $^{13}C\{^1H\}$ NOE for LSIII at 25° C, pH 4.6. The shaded regions correspond to loop I (residues 6−10), loop II (residues 26−37), and loop III (residues 48−52).

Model-Free Analysis. Initial estimates of the overall correlation time τ_m were made using the ratio R_2/R_1, excluding residues exhibiting large heteronuclear NOEs or residues with R_2/R_1 ratios differing from the mean by more than one standard deviation (*21*). A value of 4.6 ns was obtained assuming isotropic rotational diffusion. This agrees well with the value of 4.8 ns reported for cardiotoxin II based on ^{13}C relaxation (*42*) but disagrees with the value of 3.7 ns reported for toxin α based on ^{15}N relaxation (*43*). Differences in R_2/R_1 ratios obtained from ^{13}C and ^{15}N relaxation measurements of calbindin D9k were observed by Lee et al. (*44*) and were attributed to the difference in solvent viscosity between H_2O, in which ^{15}N data are acquired, and D_2O, in which ^{13}C data are typically obtained. In accord with this observation, hydrodynamic modeling (as described above) using the viscosity for D_2O gave a correlation time of 4.58 ns, in excellent agreement with the experimental estimate. Using the viscosity for H_2O rather than for D_2O yields a value of 3.65 ns, in agreement with the result for toxin α. The rotational diffusion anisotropy $2D_z/(D_x + D_y)$ was 1.12 with D_x/D_y equal to 1.13. Fitting the relaxation parameters using axial or anisotropic diffusion models (*44*) did not provide a statistically significant improvement in the fit over the isotropic model. Although it has been shown that in certain cases the neglect of anisotropy can result in artifactual R_{ex} terms in an "extended model-free" analysis of relaxation data (*45*), the small rotational diffusional anisotropy predicted

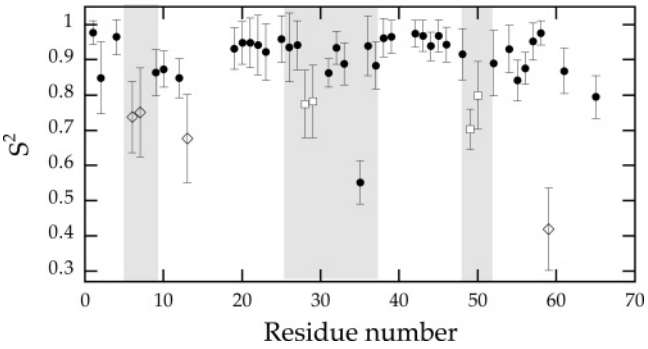

FIGURE 5: Order parameters derived from $^{13}C_\alpha$ relaxation rates for LSIII. The filled circles denote residues for which the simple dynamical model consisting of an overall correlation time and an order parameter adequately fit the relaxation data. Open diamonds and squares denote residues for which models incorporating additional parameters were required to fit the relaxation data. Diamonds denote an exchange term, and squares denote an effective internal correlation time.

from the hydrodynamic calculations indicates that the isotropic model is appropriate.

Generalized order parameters (S^2) derived from the model-free analysis are shown in Figure 5. Data for 33 residues were satisfactorily fit with the simple dynamical model including only the generalized order parameter and the overall isotropic correlation time. More complex models that included an internal correlation time and an exchange term did not improve these fits in a statistically significant way. The average value of the order parameters for these residues is 0.92, with a standard deviation of 0.05, indicating that these residues are not highly flexible and that the time scale of internal motion is rapid, <20 ps.

Relaxation data from four residues that gave unsatisfactory fits to the single-parameter model were adequately modeled by including an internal correlation time. Ala 28 and Trp 29, located at the end of loop II, had τ_e values of 75.6 and 342.9 ps, respectively, and gave order parameters smaller (0.78) than those found for residues in elements of regular structure. Surface-exposed sites in loop III (Asn 49 and Thr 50) also exhibited smaller order parameters (0.70 and 0.80) with τ_e values of 64.7 and 307.7 ps, indicating significant rapid internal motion.

Four residues required the inclusion of both an internal correlation time τ_e and an exchange parameter R_{ex} to satisfactorily fit the relaxation data. Residues Pro 7, His 8, and Cys 13, located in loop I, had R_{ex} values of 7.1, 7.1, and 10.5 s^{-1}, with order parameters 0.74, 0.75, and 0.68 respectively, indicating significant internal motion at these sites. Ala 59 had R_{ex} and S^2 values of 15.7 s^{-1} and 0.42, indicative of more extensive motion.

Concordance of the Relaxation Measurements and the Solution Structure Ensemble. The order parameters are generally consistent with the solution structure ensemble and support the hypothesis of rigid-body motion of loop II. The regions of regular secondary structure comprising the three-stranded antiparallel β-sheet (residues 19−25, 37−41, and 51−58) are well ordered in the solution structure (average backbone RMSD of 0.26 Å) and also exhibit large (average = 0.93) order parameters. Areas of the solution structure which were more disordered were mostly in the solvent-exposed tips of the loops. The end of loop I, including residues 5−9, is significantly disordered in the solution structure, and relaxation data for residues in this region (Asn 6 and Pro 7) yielded low order parameters. The turn leading into the middle β-strand is also disordered, consistent with the low order parameter found for Cys 13. Residues 49 and 50 near the tip of loop III also have lower than average order parameters and lie in the disordered region of the structure at the tip of loop III. Most of these residues also exhibited low order parameters, indicating that the disorder in the structure is largely due to internal molecular dynamics. The corresponding residues in the crystal structure of the homologous protein α-cobratoxin (*3*) gave a pattern of Debye−Waller factors quite similar to that of the order parameters we determined for LSIII. All of the residues that required more than an overall correlation time and an effective order parameter to adequately fit the relaxation data are located in solvent-exposed loops or the C-terminus, where proximity to the protein surface enables more extensive motion than for residues in the protein core.

For a few residues, the agreement between the backbone RMSD of the solution structures and order parameters was less satisfactory. Alanine 59, located at the C-terminal end of the third β-strand, was well ordered in the structure ensemble, with a backbone RMSD of 0.68 Å, yet gave an exceptionally low order parameter of 0.42. This residue gave an R_1 value of 0.72 s^{-1}, significantly slower than other residues, and was the only residue for which the 3 s recycle delay time was less than $3T_1$. Inadequate recycle delays usually result in an overestimate of the relaxation rate (*46*), however, suggesting that the true value may be lower. In any event, the order parameter suggests an amplitude of motion greater than that expected from the RMSDs based on the solution structure ensemble. Conversely, residues 31, 32, and 33 at the end of loop II show fairly large RMSDs in the solution structure but give order parameters larger than expected, in the range of 0.87−0.94, with relaxation rates similar to those found in elements of secondary structure.

Molecular Dynamics Simulation. After solvation and minimization of the starting structure (as described in Materials and Methods), the resulting structure differed slightly from the starting configuration, with an RMSD for the backbone atoms of 2.3 Å. Nearly all of this difference could be attributed to residues that were poorly defined in the solution structure ensemble. In contrast, residues belonging to elements of regular secondary structure, which were narrowly distributed in the solution ensemble, drifted by just 0.7 Å on average. During the 1.438 ns of the trajectory used for analysis the structure was relatively stable, drifting just 0.7 Å (backbone RMSD). The radius of gyration was also stable over this time interval at 12.39 ± 0.1 Å, only slightly expanded from the initial value of 11.9 Å. This difference is typical of comparisons of MD simulations performed in vacuo (as for most structure determinations) and with explicit solvent (*47*). In vacuum simulations, charged side chains frequently collapse on the surface, forming salt bridges with other charged surface residues, whereas in simulations with explicit solvent, charged side chains frequently stick out, solvated by the solvent dipoles and increasing the radius of gyration. Specific residues exhibiting the largest differences from the starting conformation were 26−37 (loop II) and those near the C-terminus.

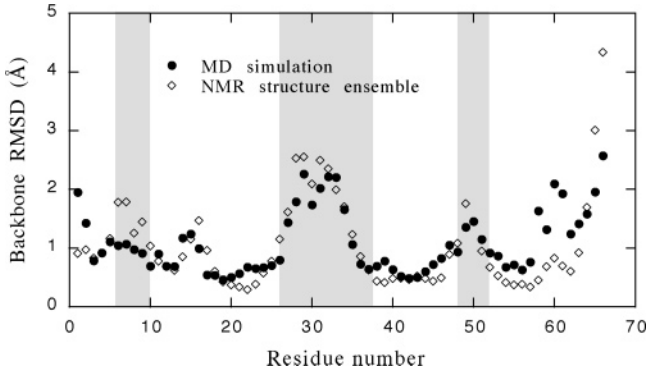

FIGURE 6: Comparison of backbone heavy atom RMS displacements calculated from the ensemble of solution structures (*2*) with those obtained from the molecular dynamics trajectory.

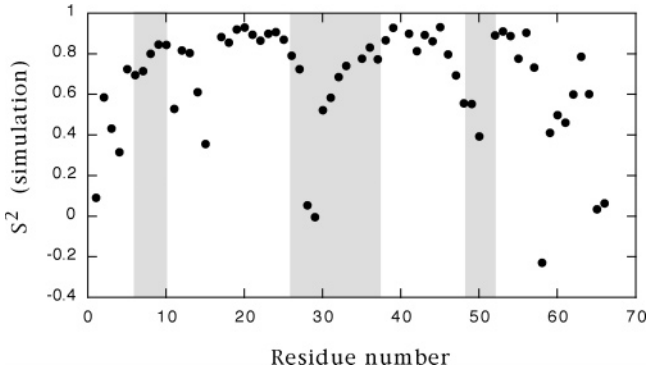

FIGURE 8: Values of the $^{13}C_\alpha-H_\alpha$ internuclear dipole correlation function at $\tau = 50$ (open diamonds), 300 (open circles), and 400 (filled circles) ps.

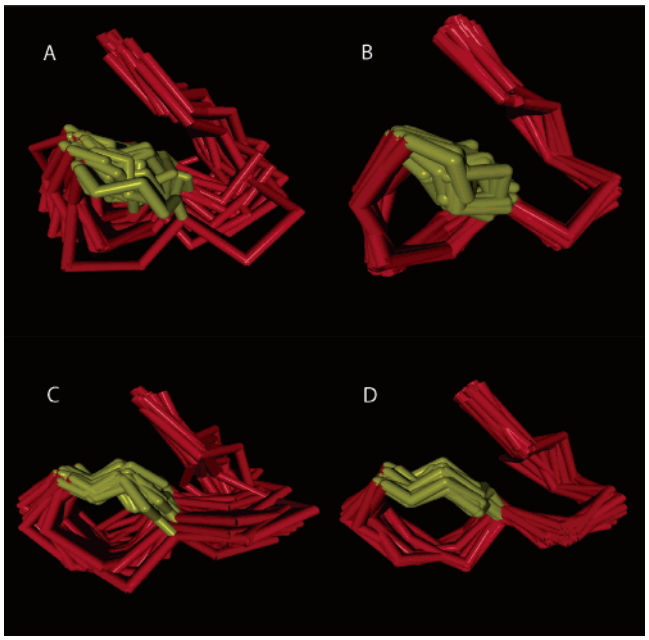

FIGURE 7: Superimposed C_α traces for loop II (residues 26−37) of LSIII from the solution structure ensemble (*2*) (A and B) and from the MD simulation (C and D), based on alignment of the structures using backbone heavy atoms for residues 1−26 and 37−62 (panels A and C) and based on backbone heavy atoms from the loop, residues 27−36 (panels B and D). The narrow distribution in panels B and D indicates that much of the apparent disorder in panels A and C arises from rigid-body displacement of the loop.

Concordance of the MD Simulation and the Solution Structure Ensemble. The range of conformations in the solution structure ensemble and the MD simulation are in excellent agreement, with the exception of those near the N- and C-termini. Backbone RMSDs for the MD trajectory are compared to those calculated from the ensemble of NMR structures in Figure 6. The extent of local order in loop II present in the NMR ensemble is mirrored in the MD simulation, as shown by comparison of globally and locally aligned conformations of the loop (Figure 7). While prior investigations of the relative extent to which MD simulations and NMR ensembles sample the thermally accessible conformation space of a protein have reached different conclusions (*48*, *49*), we speculate that the level of agreement we observe between the MD simulation and the NMR ensemble reflects in part the relatively low number of experimental restraints derived from homonuclear NMR experiments (~8 restraints per residue). However, there are many other factors that influence the distribution of conformations in a simulation (nature of the force field, explicit vs implicit solvent, polarizability) or structure ensemble (distribution of restraints, form and magnitude of the restraint potential) that have not been fully investigated.

Concordance of the MD Simulation and the Relaxation Measurements. In the simple model-free formalism of Lipari−Szabo, the order parameter is interpreted as the plateau value of the dipole correlation function resulting from fluctuations that are rapid relative to the molecular rotational correlation time. Case recently reviewed the challenges involved in computing order parameters from MD simulations, such as incomplete convergence and nonmonotonic decay of the dipole correlation function (*50*). Although the short extent of the MD simulation precludes deriving reliable statistics for fluctuations occurring with a characteristic time longer than about 500 ps, or one-third the simulation length, it is nevertheless instructive to compare the values of the dipole correlation function at fixed time lags in order to gain qualitative insight into the relaxation behavior predicted by the simulation, while recognizing that in many instances the computed dipole correlation functions have not reached a plateau. Values of the dipole correlation function at 50, 300, and 400 ps are shown in Figure 8. Although the correlation functions for relatively flexible regions of the protein do not converge on the time scale of the trajectory, the values at 400 ps nonetheless serve as reasonable qualitative indicators of the influence of internal motions on ^{13}C relaxation rates and correlate rather well with the pattern of relative mobility inferred from the measured relaxation rates. Residues for which the dipole correlation function is well converged during the simulation are those for which all three values are similar, and these correspond to order parameter values of 0.9 and greater. Also apparent in Figure 8 are residues for which the decay is nonmonotonic, such as residues 30−34 in loop II.

Characterization of the Hinge Dynamics. Angular order parameters (*40*) reflecting the width of the dihedral angle distribution (values close to 1 indicate a narrow distribution, a value of 0 indicates a uniform distribution) for the backbone ϕ and ψ dihedral angles are shown in Figure 9. The extent of the backbone dihedral angle fluctuations confirms the rigid-body character of the dynamics of loop II and indicates

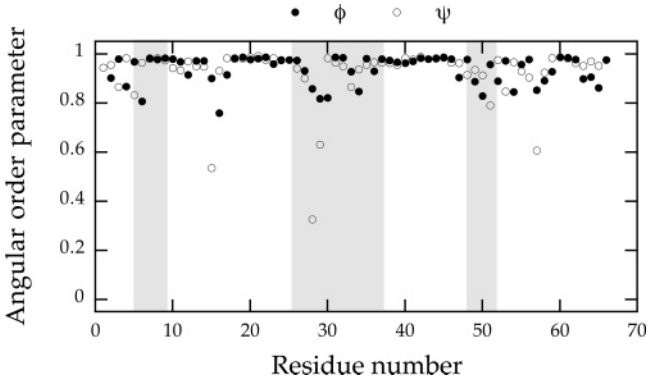

FIGURE 9: Angular order parameters computed from the MD simulation for backbone ϕ and ψ dihedral angles.

that the hinge is delocalized, involving several rotatable bonds. Six backbone dihedral angles at the end of loop II, from 30 ψ to 33 ϕ, are well ordered in the simulation, providing remarkable agreement with the large order parameters observed for residues 31, 32, and 33. The disordered dihedral angles flanking this stretch indicate that the hinge is not comprised of individual dihedral angles but involves concerted rotations of several backbone bonds. The hinge thus more closely resembles an articulated hinge, with multiple moving parts, than a simple hinge.

We characterized the collective motion of loop II by fitting planes to the C_α atoms from the β-sheet (residues 20−25, 37−39, 53−56) and loop II (residues 27−34) and computing the fluctuations of the angle between the planes. The angular fluctuations and decay of angular correlation (eq 3) are shown in Figure 10. During the MD simulation the average angle between the planes is 48° and the standard deviation is 12°, but the time course of the angle and the autocorrelation make it clear that the full range of loop motion is undersampled during the trajectory. There is a rapidly decaying component in the angular correlation, with a time scale around 100−200 ps, that corresponds to low-amplitude, high-frequency angular fluctuations of the loop. Large amplitude fluctuations of the angle occur on a slower time scale that is incompletely averaged during the time spanned by the 1.5 ns trajectory. Rigid-body motion of the loop is possibly subject to viscous damping by the solvent and requires correlated fluctuations of residues comprising the "hinge", and thus it is not surprising that the time scale for the large fluctuations approaches or even exceeds that of overall tumbling. The angle between the planes spans more than 65° during the simulation. The collective nature of the hinge angular fluctuations is emphasized by comparing the decay of angular correlation for the hinge with those of individual dihedral angles comprising the hinge (Figure 11), which decay far more rapidly.

Concordance with Relaxation Studies on Other Neurotoxins. Inagaki et al. (*51*) reported ^{13}C relaxation rates for 11 assigned methyl groups in the short neurotoxin erabutoxin *b*. They interpreted the rates using a restricted diffusion model and found large amplitudes (>50°) of restricted diffusion for Ile 40, Ile 41, and Ile 56, which are located in loops II and III, and more restricted motion (<30°) for Ile 2 and Val 65, which are located in the protein core. Guenneugues et al. (*43*) reported a more extensive ^{13}C relaxation study of the C_α resonances for toxin α from the venom of *Naja nigricollis*. The order parameters obtained from model-free analysis indicate more extensive local dynamics of the loops than the protein core. Both of these short neurotoxins lack a fifth disulfide bond bridging the end of loop II, and in the results of Guenneugues et al. there is no evidence to suggest local order at the end of loop II, as we observe in LSIII. Instead, the smallest order parameters (∼0.7) are obtained for the tip of loop II.

Biological Role of Loop II Dynamics. The thermodynamic consequences of local order at the end of loop II are readily apparent. Interfacial residues that are highly flexible in the uncomplexed state will impose an entropic penalty resulting from degrees of freedom that become restricted on binding. Quasi-rigid-body motion of locally ordered residues will result in the loss of fewer degrees of freedom, mainly those contributing to the hinge, than flexible, locally disordered residues. Consequently, the binding free energy will be more favorable for a toxin with a rigid loop than for one with a highly flexible loop. Several investigators have attempted to quantify this effect (*8*, *9*), with estimates in the range 0.8−1.7 kcal/mol (TS at 300 K) for the entropic contribution of a freely rotatable bond relative to a fully constrained bond. Thus the six constrained bonds in the end of loop II could contribute up to 10 kcal/mol to the free energy of LSIII binding to AChR, compared to six unconstrained bonds. This estimate undoubtedly represents an upper bound, because bond rotation is not completely restricted in the bound state nor completely free in the uncomplexed state. Nevertheless, the estimated bound should be more realistic for loop II in LSIII, with its bridging disulfide, than for a similar size loop lacking the disulfide bond.

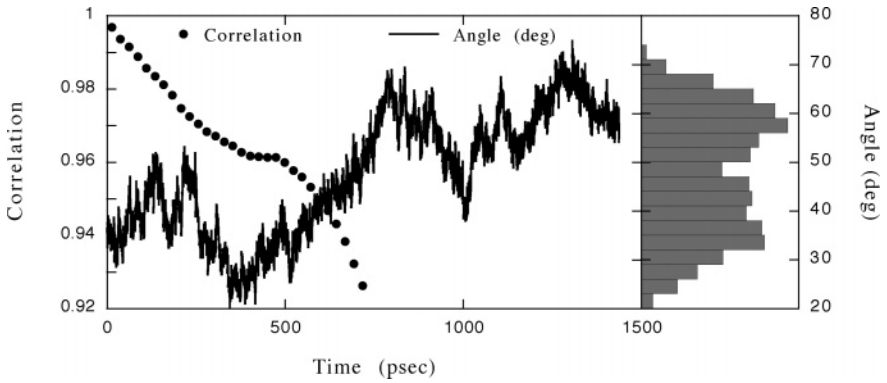

FIGURE 10: Fluctuations and correlation of the angle between planes fit to residues comprising the β-sheet (20−25, 37−39, 53−56) and loop II (27−34) during the MD simulation.

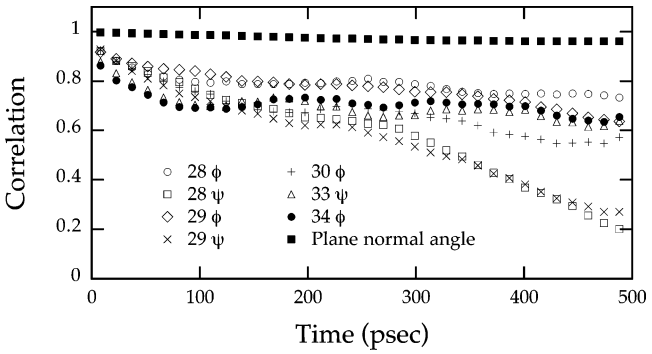

FIGURE 11: Comparison of the angular time correlation (eq 3) for the planes fit to the β-sheet and loop II with angular time correlations for individual dihedral angles contributing to the hinge motion of the loop.

Emerging details concerning the architecture of AChR (*11*) invite speculation concerning the detailed role of loop II flexibility in LSIII for binding to AChR. LSIII and related neurotoxins act as competitive inhibitors of ACh binding to AChR (*1*). Superposition of the structured region of a peptide derived from the α7 subunit of AChR in complex with α-bungarotoxin (*15*) onto the corresponding region of the crystal structure of the extracellular domain of AChR (acetylcholine-binding protein, PDB entry 1I9B) (*52*) places the binding site at the subunit interface, adjacent to the membrane, with the long axis of the toxin forming a 45° angle with respect to the pseudo-5-fold vertical axis of the receptor (Figure 9C of ref *13*). The tip of loop II extends deep into the crevice formed by the subunit interface. The ACh binding pockets, however, are located at the ends of narrow channels a few angstroms wide that lead from the vestibule in the center of the ring formed by the five subunits (*11*). LSIII, which is 25 Å wide along its narrowest dimension, is too large to enter the 20 Å diameter vestibule. Evidence that neurotoxins induce a conformational change in AChR on binding (*13*, *14*) therefore suggests that neurotoxins do not bind at the ACh binding site but instead cause conformational changes that occlude the binding site. The hinge region that connects loop II to the globular core of LSIII may allow it to remain bound as the conformational change occurs, permitting residues at the tip of the loop to remain in contact with AChR while the core moves to accommodate a change in the relative orientation of AChR subunits.

CONCLUDING REMARKS

The present study reveals that the dynamical properties of LSIII are broadly consistent with those observed for other globular proteins. For example, residues near the N- and C-termini and in extended loops exhibit lower order parameters and undergo more extensive fluctuations in the MD simulation than residues comprising secondary structure elements in the protein core. A distinguishing characteristic is the rigid-body motion of loop II. The relaxation data and MD simulation are both consistent with slow and extensive angular fluctuations of loop II with respect to the protein core. Analysis of the MD simulation indicates that the angular fluctuations of the loop involve concerted fluctuations of several backbone dihedral angles flanking the loop.

The dynamics of the central binding loop holds implications for the biological activity, through the lower entropic cost of binding to well-ordered residues in the loop and the structural plasticity afforded by a loop that samples a wide range of orientations with respect to the protein core. This plasticity can influence binding kinetics by increasing the likelihood of a productive encounter between the neurotoxin and AChR and can influence the thermodynamics by adapting to conformational change induced in the receptor. More detailed structural and thermodynamic investigations of the interaction between long neurotoxins and AChR are needed to quantify the extent to which the dynamics of the central binding loop influence their activity as neurotoxins. Complexes of neurotoxins and the extracellular domain of AChR should be amenable to investigation using relaxation-optimized methods (*53*).

SUPPORTING INFORMATION AVAILABLE

One table listing C^{α} chemical shift and relaxation parameters for LSIII at 25 °C, pH 4.6. This material is available free of charge via the Internet at http://pubs.acs.org.

REFERENCES

1. Endo, T., and Tamiya, N. (1987) Current view on the structure−function relationship of postsynaptic neurotoxins from snake venoms, *Pharmacol. Ther. 34*, 403−451.
2. Connolly, P. J., Stern, A. S., and Hoch, J. C. (1996) Solution structure of LSIII, a long neurotoxin from the venom of *Laticauda semifasciata*, *Biochemistry 35*, 418−426.
3. Betzel, C., Lange, G., Pal, G. P., Wilson, K. S., Maelicke, A., and Saenger, W. (1991) The refined crystal structure of alpha-cobratoxin from *Naja naja siamensis* at 2.4-A resolution, *J. Biol. Chem. 266*, 21530−21536.
4. Love, R. A., and Stroud, R. M. (1986) The crystal structure of α-bungarotoxin at 2.5 Å resolution: relation to solution structure and binding to acetylcholine receptor, *Protein Eng. 1*, 37−46.
5. Le Goas, R., LaPlante, S. R., Mikou, A., Delsuc, M.-A., Guittet, E., Robin, M., Charpenteir, I., and Lallemand, J.-Y. (1992) Alpha-cobratoxin: proton NMR assignments and solution structure, *Biochemistry 31*, 4867−4875.
6. Wagner, G., Hyberts, S., and Peng, J. W., (1993) Study of Protein Dynamics by NMR, in *NMR of Proteins* (Clore, G. M., and Gronenborn, A. M., Eds.) CRC Press Inc., Boca Raton, FL.
7. Dayie, K. T., Wagner, G., and Lefevre, J. F. (1996) Theory and practice of nuclear spin relaxation in proteins, *Annu. Rev. Phys. Chem. 47*, 243−248.
8. Page, M. I., and Jencks, W. P. (1971) Entropic contributions to rate accelerations in enzymic and intramolecular reactions and the chelate effect, *Proc. Natl. Acad. Sci. U.S.A. 68*, 1678−1683.
9. Searle, M. S., and Williams, D. H. (1992) The cost of conformational order: entropy changes in molecular associations, *J. Am. Chem. Soc. 114*, 10690−10697.
10. Antil-Delbeke, S., Gaillard, C., Tamiya, T., Corringer, P.-J., Changeux, J.-P., Servent, D., and Menez, A. (2000) Molecular Determinants by which a long chain toxin from snake venom interacts with the neuronal a7-nicotinic acetylcholine receptor, *J. Biol. Chem. 275*, 29594−29601.
11. Miyazawa, A., Fujiyoshi, Y., Stowell, M., and Unwin, N. (1999) Nicotinic acetylcholine receptor at 4.6 Å resolution: transverse tunnels in the channel wall, *J. Mol. Biol. 288*, 765−786.
12. Unwin, N., Miyazawa, A., Li, J., and Fujiyoshi, Y. (2002) Activation of the nicotinic acetylcholine receptor involves a switch in conformation of the alpha subunits, *J. Mol. Biol. 319*, 1165−1176.
13. Maelicke, A., Fulpius, B. W., Klett, R. P., and Reich, E. (1977) Acetylcholine receptor. Responses to drug binding, *J. Biol. Chem. 252*, 4811−4830.
14. Endo, T., Nakanishi, M., Furukawa, S., Joubert, F. J., Tamiya, N., and Hayashi, K. (1986) Stopped-flow fluorescence studies on binding kinetics of neurotoxins with acetylcholine receptor, *Biochemistry 25*, 395−404.

15. Moise, L., Piserchio, A., Basus, V. J., and Hawrot, E. (2002) NMR structural analysis of alpha-bungarotoxin and its complex with the principal alpha-neurotoxin-binding sequence on the alpha 7 subunit of a neuronal nicotinic acetylcholine receptor, *J. Biol. Chem. 277*, 12406−12417.
16. Wishart, D. S., Bigam, C. G., Yao, J., Abildgaard, F., Dyson, H. J., Oldfield, E., Markley, J. L., and Sykes, B. D. (1995) ^{1}H, ^{13}C and ^{15}N chemical shift referencing in biomolecular NMR, *J. Biomol. NMR 6*, 135−140.
17. Kay, L. E., Torchia, D. A., and Bax, A. (1989) Backbone dynamics of proteins as studied by 15N inverse detected heteronuclear NMR spectroscopy: application to staphylococcal nuclease, *Biochemistry 28*, 8972−8979.
18. Zhang, O., Kay, L. E., Olivier, J. P., and Forman-Kay, J. D. (1994) Backbone ^{1}H and ^{15}N resonance assignments of the N-terminal SH3 domain of drk in folded and unfolded states using enhanced-sensitivity pulsed field gradient NMR techniques, *J. Biol. NMR 4*, 845−858.
19. Skelton, N. J., Palmer, A. G., Akke, M., Kördel, J., Rance, M., and Chazin, W. J. (1993) Practical aspects of two-dimensional proton-detected ^{15}N spin relaxation measurements, *J. Magn. Reson. B 102*, 253−264.
20. Dayie, K. T., and Wagner, G. (1994) Relaxation-rate measurements for ^{15}N-^{1}H groups with pulsed-field gradients and preservation of coherence pathways, *J. Magn. Reson., Ser. A 111*, 121−126.
21. Kay, L. E., Nicholson, L. K., Delaglio, F., Bax, A., and Torchia, D. (1992) Pulse sequences for removal of the effects of cross-correlation between dipolar and chemical-shift anisotropy relaxation mechanism on the measurement of heteronuclear T_1 and T_2 values in proteins, *J. Magn. Reson. 97*, 359−375.
22. Palmer, A. G., Skelton, N. J., Chazin, W. J., Wright, P. E., and Rance, M. (1992) Suppression of the effects of cross-correlation between dipolar and anisotropic chemical-shift relaxation mechanisms in the measurement of spin spin relaxation rates, *Mol. Phys. 75*, 699−711.
23. Hoch, J. C. (1985) *The Rowland NMR Toolkit*, Rowland Institute for Science Technical Memorandum No. 18t, Rowland Institute for Science, Cambridge, MA.
24. Hoch, J. C., and Stern, A. S., (1996) *NMR Data Processing*, Wiley-Liss, New York.
25. Bartels, C., Xia, T.-H., Bileter, M., Güntert, P., and Wütrich, K., (1995) The program XEASY for computer-supported NMR spectral analysis of biological macromolecules, *J. Biomol. NMR 6*, 1−10.
26. Palmer, A. G., Rance, M., and Wright, P. E., (1991) Intramolecular motions of a zinc finger DNA-binding domain from Xfin characterized by proton-detected natural abundance carbon-13 heteronuclear NMR spectroscopy, *J. Am. Chem. Soc. 113*, 4371−4380.
27. Mandel, A. M., Akke, M., and Palmer, A. G., (1995) Backbone dynamics of *Escherichia coli* ribonuclease HI: correlations with structure and function in an active enzyme, *J. Mol. Biol. 246*, 144−163.
28. Lipari, G., and Szabo, A. (1982) Model-free approach to the interpretation of nuclear magnetic resonance relaxation in macromolecules. 1. Theory and range of validity, *J. Am. Chem. Soc. 104*, 4546−4559.
29. Palmer, A. G., Kroenke, C. D., and Loria, J. P. (2001) NMR methods for quantifying microsecond-to-millisecond motions in biological macromolecules, *Methods Enzymol. 339*, 204−238.
30. Palmer, A. G. (2001) NMR probes of molecular dynamics: Overview and comparison with other techniques, *Annu. Rev. Biophys. Biomol. Struct. 30*, 129−155.
31. Garcia de la Torre, J. G., and Bloomfield, V. A. (1981) Hydrodynamic properties of complex, rigid, biological macromolecules: theory and applications, *Q. Rev. Biophys. 14*, 81−139.
32. Cho, C. H., Urquidi, J., Singh, S., and Robinson, G. W. (1999) Thermal offset viscosities of liquid H_2O, D_2O, and T_2O, *J. Phys. Chem. B 103*, 1991−1994.
33. Pearlman, D. A., Case, D. A., Caldwell, J. W., Ross, W. S., Cheatham, T. E., III, Ferguson, D. M., Seibel, G. L., Singh, U. C., Weiner, P. K., and Kollman, P. A. (1995) *AMBER 4.1*, University of California, San Francisco.
34. Fox, T., and Kollman, P. A., (1996) The application of different solvation and electrostatic models in molecular dynamics simulations of ubiquitin: how well is the X-ray structure "maintained"?, *Proteins 25*, 315−334.
35. Cornell, W. D., Cieplak, P., Bayly, C. I., Gould, I. R., Merz, K. M., Jr., Ferguson, D. M., Spellmeyer, D. C., Fox, T., Caldwell, J. W., and Kollman, P. A. (1995) A second generation force field for the simulation of proteins, nucleic acids, and organic molecules, *J. Am. Chem. Soc. 117*, 5179−5197.
36. Darden, T. A., York, D. M., and Pedersen, L. G. (1993) Particle mesh Ewald: an N*log(N) method for computing Ewald sums, *J. Chem. Phys. 98*, 10089−10092.
37. Berendsen, H. J. C., Grigera, J. R., and Straatsma, T. P. (1987) The missing term in effective pair potentials, *J. Phys. Chem. 91*, 6269−6271.
38. Berendsen, H. J. C., Postma, J. P. M., and Van Gunsteren, W. F., DiNola, A., and Haak, J. R. (1984) Molecular dynamics with coupling to an external bath, *J. Chem. Phys. 81*, 3684−3690.
39. Ryckaert, J.-P., Ciccotti, G., and Berendsen, H. J. C. (1997) Numerical integration of the Cartesian equations of motion of a system with constraints: Molecular dynamics of *n*-alkanes, *J. Comput. Phys. 23*, 327−341.
40. Hyberts, S. G., Goldberg, M. S., Havel, T. F., and Wagner, G. (1992) The solution structure of eglin c based on measurements of many NOEs and coupling constants and its comparison with X-ray structures, *Protein Sci. 1*, 736−751.
41. Marion, D., Driscoll, P. C., Kay, L. E., Wingfield, P. T., Bax, A., Gronenborn, A. M., and Clore, G. M. (1989) Overcoming the overlap problem in the assignment of 1H NMR spectra of larger proteins by use of three-dimensional heteronuclear ^{1}H−^{15}N Hartmann−Hahn-multiple quantum coherence and nuclear Overhauser-multiple quantum coherence spectroscopy: application to interleukin 1 beta, *Biochemistry 28*, 6150−6156.
42. Lee, C. S., Kumar, T. K., Lian, L. Y., Cheng, J. W., and Yu, C. (1998) Main-chain dynamics of cardiotoxin II from Taiwan cobra (*Naja naja atra*) as studied by carbon-13 NMR at natural abundance: delineation of the role of functionally important residues, *Biochemistry 37*, 155−164.
43. Guenneugues, M., Gilquin, B., Wolff, N., Menez, A., and Zinn-Justin, S. (1999) Internal motion time scales of a small, highly stable and disulfide-rich protein: a ^{15}N, ^{13}C NMR and molecular dynamics study, *J. Biomol. NMR 14*, 47−66.
44. Lee, L. K., Rance, M., Chazin, W. J., and Palmer, A. G., III (1997) Rotational diffusion anisotropy of proteins from simultaneous analysis of ^{15}N and ^{13}C alpha nuclear spin relaxation, *J. Biomol. NMR 9*, 287−298.
45. Schurr, J. M., Babcock, H. P., and Fujimoto, B. S. (1994) A test of the model-free formulas. Effects of anisotropic rotational diffusion and dimerization, *J. Magn. Reson. B 105*, 211−224.
46. Canet, D., Levy, G. C., and Peat, I. R. (1975) Time saving in ^{13}C spin−lattice relaxation measurements by inversion−recovery, *J. Magn. Reson. 18*, 199−204.
47. van Gunsteren, W. F., and Karplus, M. (1981) Effect of constraints, solvent and crystal environment on protein dynamics, *Nature 293*, 677−678.
48. Berndt, K. D., Güntert, P., and Wüthrich, K. (1996) Conformational sampling by NMR solution structures calculated with the program DIANA evaluated by comparison with long-time molecular dynamics calculations in explicit water, *Proteins 24*, 304−313.
49. Philippopoulos, M., and Lim, C. (1999) Exploring the dynamic information content of a protein NMR structure: comparison of a molecular dynamics simulation with the NMR and X-ray structures of *Escherichia coli* ribonuclease HI, *Proteins 36*, 87−110.
50. Case, D. A. (2000) Molecular dynamics and NMR spin relaxation in proteins, *Acc. Chem. Res. 35*, 325−331.
51. Inagaki, F., Miyazawa, T., Tamiya, N., and Williams, R. J. P. (1982) Structural dynamics of erabutoxin b. A ^{13}C nuclear magnetic resonance relaxation study of methyl groups, *Eur. J. Biochem. 123*, 99−104.
52. Brejc, K., van Dijk, W. J., Klaassen, R. V., Schuurmans, M., van der Oost, J., Smit, A. B., and Sixma, T. K. (2001) Crystal structure of an ACh-binding protein reveals the ligand-binding domain of nicotinic receptors, *Nature 411*, 269−276.
53. Salzmann, M., Pervushin, K., Wider, G., Senn, H., and Wüthrich, K. (1998) TROSY in triple-resonance experiments: new perspectives for sequential NMR assignment of large proteins, *Proc. Natl. Acad. Sci. U.S.A. 95*, 13585−13590.

BI034687M